ADVANCED MATERIALS INTERFACES
Open Access
www.advmatinterfaces.de

Coupled Solid-State Diffusion of Li^+ and O^{2-} During Fabrication of Ni-Rich NMC Thin-Film Cathodes Resulting in the Formation of Inactive Ni_2O_3 and NiO Phases

*Sameer Rodrigues, Louis De Taeye, and Philippe M. Vereecken**

Ni-rich $Li(Ni_{1-x-y}Mn_xCo_y)O_2$ (NMC) is an attractive cathode material for Li-ion batteries due to its high practical capacity (>200 mAh g^{-1}). However, it is plagued by stability issues that, over multiple cycles or prolonged storage in air, degrade the material and decreases its electrochemical performance. A thin-film model system can be used to simplify the cathode by omitting all passive components and electrode porosity and allow for an in-depth analysis on the interfacial reactions that initiate the material degradation. In this work, the reactions occurring during the fabrication of thin film NMC are investigated. A lot of these reactions stemmed from the loss of active material from the film toward the substrate during annealing. Methods are then devised to reduce the unwanted reactions occurring during annealing. These included lowering the annealing temperature, compensating for material loss, as well as depositing a diffusion barrier between the substrate and NMC film. The findings in this paper outline the various conditions that affect the preparation of thin-film NMC and give readers an overview of reactions to consider when developing thin-film battery materials.

1. Introduction

Lithium-ion batteries have become a prominent power source for various electronic devices, ranging from smartphones to electric vehicles. The cathode material in these batteries plays a pivotal role in maintaining the performance and stability of the battery. Cathode materials comprising the $Li(Ni_xMn_yCo_z)O_2$ (NMC) stoichiometry have emerged as promising candidates due to their high capacity.[1] However, this comes with a trade-off, while increasing the nickel content enhances the capacity, it concurrently diminishes the stability of the material. It is known that in its charged state, the highly reactive Ni^{4+} is formed. This can then oxidize the flammable electrolyte, to form the more stable Ni^{2+}, releasing oxygen in the process.[2] This results in thermal runaway and the eventual failure of the battery.[2] As a result, the capacity rapidly decreases over multiple cycles. As the nickel content increases, the amount of oxygen released and thermal runaway has been shown to increase, thereby decreasing the safety of Ni-rich cathode materials.[2] Therefore, during battery operation, the increased capacity that was initially gained from the increasing nickel content is negated due to the deterioration of the material, restricting their potential applications.[3–9]

Apart from the reaction of Ni^{4+} with the electrolyte, the transition metals within NMC can also move from the transition metal sites to the lithium sites within the NMC lattice.[10] The transition metals that occupy the lithium sites then hinder the diffusion of Li^+ ions. This process can occur during delithiation, either via electrochemical charging or via storage in humid environments, whereby Li^+ ions are extracted from the material to form Li_2CO_3 on the surface.[3,10] The movement of transition metals to the lithium sites also leads to the structural transition of NMC from the layered phase to a spinel phase, and eventually a rock salt phase, where each transition metal is in its +2 oxidation state.

Many of these concerns regarding stability and structural transformation originate from an initial alteration in the surface chemistry, morphology, and structure, during storage, and high voltage operation. This suggests that even though the rock salt phase takes up about 10 – 25 nm, it is enough to increase the impedance of Li^+ ions between the electrode/electrolyte interface.[11,12] In order to gain a more comprehensive understanding of the surface reactivity and its impact on the electrochemical behavior of NMC cathodes, it is beneficial to isolate surface reactions from those taking place in the bulk material.

S. Rodrigues, L. De Taeye, P. M. Vereecken
imec
Kapeldreef 75, Leuven 3001, Belgium
E-mail: Philippe.Vereecken@imec.be
S. Rodrigues, L. De Taeye, P. M. Vereecken
EnergyVille
Thor Park 8310, Genk 3600, Belgium
S. Rodrigues, P. M. Vereecken
KU-Leuven
Centre for Membrane Separations, Adsorption, Catalysis, and Spectroscopy for Sustainable Solutions
Celestijnenlaan 200f - box 2454, Leuven 3001, Belgium

The ORCID identification number(s) for the author(s) of this article can be found under https://doi.org/10.1002/admi.202400911

DOI: 10.1002/admi.202400911

One possible approach to accomplish this is by using a thin-film model system, which provides a high surface area-to-volume ratio and a well-controlled single interface, allowing for more in-depth investigations of interfacial reactions at the NMC surface.[13–16] The planar form factor also facilitates in depth analysis of the material, by enabling the utilization of a wider array of characterization techniques that could not be utilized to analyze a powder-based cathode material.

Due to the high surface-to-volume ratio in the thin-film system, reactions taking place on the surface will be accentuated in comparison to that of powder-based cathodes. Therefore, the properties of the thin film system are significantly influenced by external conditions during fabrication, storage and measurement.[13–18] For instance, annealing is a critical step in the development of thin-film NMC cathodes, as it enables the formation of a well-defined crystalline structure. Moreover, the annealing conditions can affect the material's homogeneity and composition, both of which can substantially affect the cathode's electrochemical properties. Previous literature shows that NMC thin films perform best in its crystalline form, after undergoing an annealing treatment, however there is no consensus on what the optimal annealing temperature is refs. [17–19]. In this paper, we investigated the impact of the annealing temperature on the structure, composition, morphology, and electrochemical performance of thin film NMC cathodes.

It is also widely mentioned that lithium is lost from the film during the annealing treatment, due to it being volatile at the high temperatures required for annealing.[13,20,21] While our results confirm a decrease in the lithium content after annealing, this is also accompanied by a decrease in oxygen. In addition to this decrease, we notice a volume expansion of the platinum substrate after annealing, indicating that lithium and oxygen do not necessarily move out of the material exclusively via evaporation, but can also react with the platinum substrate to form lithium platinates. As Li_2CO_3 has been used as a lithium precursor for NMC cathodes,[22] we have examined the influence of a sacrificial Li_2CO_3 layer on the as-deposited film, with the objective of compensating for material loss during the annealing process. We also investigated the use of a diffusion barrier in between the NMC and Pt layers to slow the rate of reaction between these layers during the annealing process. Our findings in this article contribute to the understanding of how different preparation conditions affect the final film and provide guidelines on how to fabricate thin-film NMC cathodes with better control.

2. Results and Discussions

2.1. Effect of Annealing Temperature

NMC thin films of 125 nm were deposited by RF-sputtering on Pt coated $TiO_2/SiO_2/Si$ samples at ambient temperature from a $LiNi_{0.8}Mn_{0.1}Co_{0.1}O_2$ (NMC811) target in Ar plasma. The cross-sectional and top-down view SEM scans of the as-deposited film in **Figure 1**a,d shows a continuous, dense film with a columnar-type growth on top of the 70 nm Pt current collector. The ratio of Ni:Mn:Co transition metals was found, from EDX, to be 0.77:0.03:0.20 (see Figure S1, Supporting Information), hence the composition of the film deviated somewhat from the NMC811 target being Co rich and Mn poor. The full chemical composition with Li and O content was determined by ERD measurements, which gave additional compositional information on the element distribution throughout the depth of the film and on impurities such as H and C as shown in Figure 1g. From the bulk region in the ERD profile and the transition metal ratio obtained from EDX, the film composition is estimated to be $Li_{0.9}H_{0.2}(Ni_{0.77}Mn_{0.03}Co_{0.2})O_{2.5}$. From the ratio of transition metal to oxygen, it can be inferred that the film was somewhat rich in oxygen. Interestingly, the film contained hydrogen or H^+ next to the Li^+ ions. The film exhibited a thick surface region comprising Li, C, H, and O, consistent with the surface layer seen in the cross-sectional SEM image (Figure 1a) which is then most likely composed of Li_2CO_3 and LiOH, and is about 48 nm thick. While Li_2CO_3 and LiOH are commonly "seen" on the surface of NMC cathodes that are exposed to air,[2,4,6,19] however, it has not yet been shown that this layer can be thick enough to be visible with SEM. The hydrogen, which is suspected to originate from exposure to humid air, is not only limited to the surface but also permeates into the bulk of the film. This suggests that the NMC is protonated as a result of the formation of the surface layer, whereby Li^+ is extracted from the (bulk) material, to maintain charge-neutrality within the bulk of the film. This leads to the formation of transition metal oxyhydroxides within the bulk.

The 2theta-omega and the grazing incidence XRD scans of these films are shown in **Figure 2**a,b respectively. The as deposited films are amorphous, with no peaks being attributed to the NMC film, neither in Bragg-Brentano nor grazing incidence geometry. To crystallize the film, anneals are typically done in an oxygen atmosphere to counter oxygen loss.[23] Therefore, in situ XRD was performed during heating of the sample in oxygen atmosphere to determine its crystallization temperature (shown in Figure S2, Supporting Information). To establish the onset of crystallization, the most intense plane, (003), in the range of 17.82° and 18.44° in 2θ, was monitored utilizing a ramp rate of 10°C min^{-1}. The (003) peak appeared at 700°C, and subsequently decreased at higher temperatures to disappear at 900°C, potentially suggesting an additional phase change upon further temperature increase. Therefore, 700°C was set as the annealing temperature for crystallization. The films were annealed at 700°C for 10 min, with a ramp rate of 10°C min^{-1} during heating (*NMC-700C*). However, as there was no active cooling, the temperature decreased at a much slower rate (see Figure S3, Supporting Information).

The 2theta-omega ex-situ XRD for the *NMC-700C* film shows peaks that can be attributed to NMC. However, these peaks would also arise from Li_2PtO_3, which can form by reaction of Li_2O (or Li_2CO_3) and PtO_2 at the Pt substrate, as shown from XRD of Li_2CO_3 annealed on a Pt substrate in O_2 at 700°C (case 5 in Figure 2). Therefore, to confirm that the NMC film was crystalline, NMC was deposited on a SiO_2 substrate and annealed at 700°C to eliminate reactions with Pt. Each sample was also measured with a grazing incidence geometry to reduce the influence of substrate peaks. From Figure 2b, it is clear that a lot of the NMC peaks overlap with those of Pt and Li_2PtO_3, making it difficult to definitively confirm whether the active material is crystalline. Aligning the diffraction peaks of *NMC-700C*, *NMC-SiO_2-700C* and *Li_2PtO_3-Pt-700C*, it can be seen that the NMC peak that does not overlap with the substrate is the one around 64.38°, confirming that crystalline NMC is present in the film. Additionally,

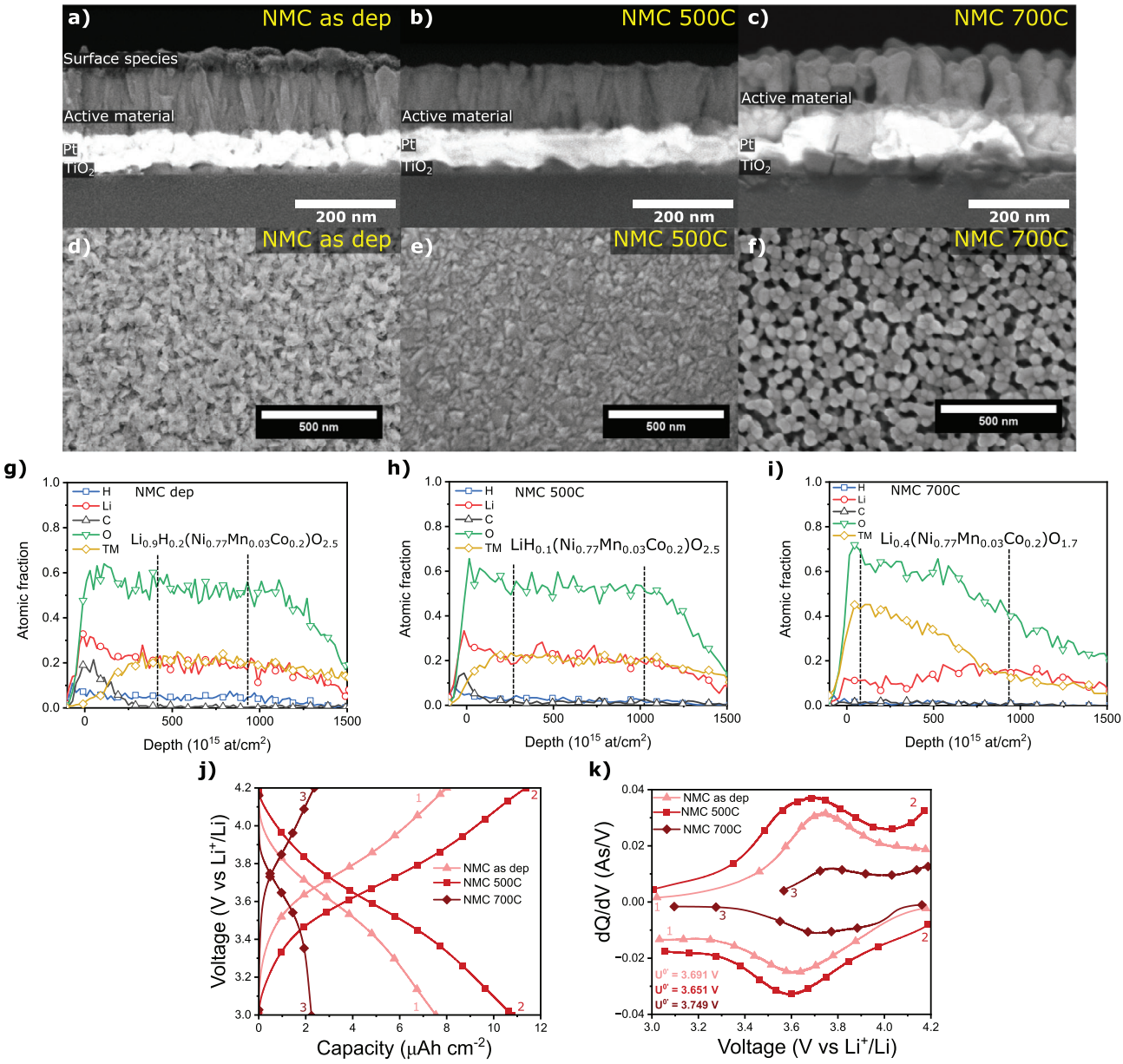

Figure 1. a–f) Cross-sectional and top-down SEM images of (a, d) as deposited NMC (*NMC-as-dep*), (b,e) NMC annealed at 500°C for 1 h in O_2 (*NMC-500C*) and (c,f) NMC annealed at 700°C for 10 min in O_2 (*NMC-700C*). ERD depth scans of (g) *NMC-as-dep*, h) *NMC-500C* and (i) *NMC-700C*. An approximation of the composition was determined from the atomic fraction between the dashed lines. Surface species that are rich in carbon and hydrogen are present in *NMC-as-dep* and to a lesser extent in *NMC-500C*. The lithium content in *NMC-700C* is low in the upper regions of the film and increases as the scan depth increases, signifying movement of species toward the substrate. Comparison of the voltage versus capacity and the corresponding dQ/dV plots of (j,k) *NMC-as-dep*, *NMC-500C*, and *NMC-700C* during constant current charge–discharge measurements. The charge discharge measurements were conducted after three cyclic voltammetry measurements at 1 mV s^{-1}. The figure depicts the 3rd constant current charge–discharge cycle. The charge–discharge measurements were performed at a current density of 0.349 μA cm^{-2}. The formal potentials ($U^{0\prime}$) of the third charge–discharge cycle of each film are indicated in the dQ/dV scans.The charge–discharge and dQ/dV curves are labeled 1, 2, and 3 to represent *NMC-as-dep*, *NMC-500C* and *NMC-700C*, respectively.

the presence of Li_2PtO_3 diffraction peaks suggest a reaction between the active material and Pt current collector. This reaction will be further studied in the following sections.

The SEM cross-sectional and top-down views of the *NMC-700C* sample are shown in Figure 1c,f. The film has become porous and shows a pillar-like morphology. Interestingly, the active layer has decreased in thickness from 125 to 110 nm which, together with the introduced porosity, suggests a loss in active material. In addition, a volume expansion of the Pt film is observed, i.e., from a thickness of 73 nm before annealing to 95 nm after annealing, indicating that a reaction takes place between the NMC and Pt films during annealing. Note that also some

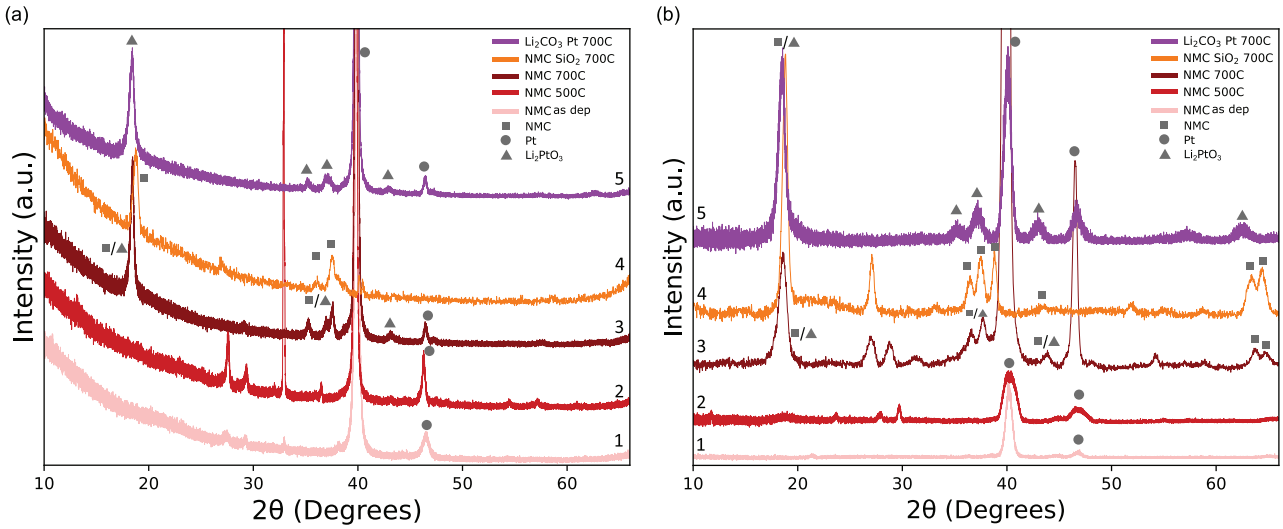

Figure 2. XRD diffractograms of (1) *NMC-as-dep*, (2) *NMC-500C*, (3) *NMC-700C*, (4) *NMC-SiO_2-700C* and (5) *Li_2CO_3-Pt-700C* using a (a) 2theta-omega and (b) grazing incidence geometry. The peaks attributed to NMC, Pt and Li_2PtO_3 are assigned via the symbols shown in the legend. These were based on the ideal crystalline structure of each species, shown in Figure S4 (Supporting Information).

damage and cavities are seen in the underlying TiO_2 and SiO_2 layers. A film porosity of about 20% is estimated from the contrast in the top-down SEM images. Further, the Li_2CO_3 film of the as-deposited film is no longer observed on top of the annealed film. The ERD scan in Figure 1i confirms that, in contrast to *NMC-as-dep*, there was no Li_2CO_3 or LiOH on the surface of *NMC-700C*. It is suspected that the Li_2CO_3 has recombined with the active film during anneal, but importantly it can be concluded also that the crystallization stabilized the film as no such Li_2CO_3 film was reformed after exposure to air. The solid-state reactions at the Li_2CO_3/NMC and NMC/Pt interfaces clearly show also in the obtained ERD profile as the composition now varies throughout the full depth of the film and below. The NMC film (top) is significantly Li depleted with a Li content four times lower than that of the transition metal (whereas 1:1 for *NMC-as-dep*). This suggest Li_2O is diffusing out of the film toward the substrate, resulting in transition metal oxides within the film, likely in the form of NiO.[24] Furthermore, the transition metal content decreases steadily. Interestingly, the lithium content increases again deeper into the sample, most probably into the Pt film, suggesting a reaction between Pt and Li_2O, as was seen via XRD. The oxygen content is relatively constant in the active material, and drops significantly when the Pt interface is passed, even though still in excess of 20% even at the end of the profile, confirming oxides are formed. Therefore, it can be inferred that Li_2O, in conjunction with oxygen, reacts with the substrate during the annealing process. It should also be noted that based on the SEM results, the *NMC-700C* film is quite porous. The presence of pores and voids in the film complicates the ERD analysis. The primary ion beam can penetrate through the pores and generate recoiled ions from within the bulk of the layer, making accurate compositional analysis throughout the depth difficult. Such effects can lead to sloped profiles but the general trends in ratio and interface transitions hold.

To try reducing the reaction between the NMC and Pt, annealing at a lower temperature of 500°C was attempted. Additionally, the samples, labeled as *NMC-500C*, were annealed inside the deposition tool preventing exposure to air. Figure 1b,e, respectively, show the cross-sectional and top-down SEM views of *NMC-500C*. The film has maintained the uniform and a columnar morphology of *NMC-as-dep*. Notably, also the Pt film maintained the same thickness. Interestingly, the Li_2CO_3/LiOH surface layer on this film was much thinner than that of *NMC-as-dep*, even though they were exposed to air for similar durations. This suggests that the 500°C annealing has a stabilizing effect on the amorphous NMC films, decreasing their affinity to react with air, even though less than for the crystalline *NMC-700C* films (compare also the surface layers in ERD spectra). The bulk composition of *NMC-500C* from ERD has not changed from the as-deposited films except for a decrease in hydrogen content, and slightly higher lithium content as the *NMC-500C* film did not lose as much lithium as *NMC-as-dep* to form Li_2CO_3 on the surface. Importantly, the ERD spectra do not show any loss of NMC material into the Pt film, confirming no reaction has taken place. However, the films are amorphous-like as the XRD showed only peaks for the substrate (Figure 2).

The electrochemical properties of the as-deposited, amorphous-stabilized (500°C) and porous crystalline (700°C) films were characterized by galvanostatic charge–discharge measurements at 0.2C (Figure 1j) and cyclic voltammetry (Figure S5, Supporting Information). The corresponding dQ/dV plots show the difference in peak position and intensity. The as-deposited NMC film already displayed distinct discharge-capacity properties with typical NMC voltage-capacity profile. The discharge capacity of 7.5 μAh cm^{-2} corresponds to volumetric capacity of 600 mAh cm^{-3} assuming a dense 124 nm film; i.e., a little less than half the theoretical capacity of 1330 mAh cm^{-3}. The *NMC-500C* film possessed a higher capacity of 10.8 μAh cm^{-3}, corresponding to ≈860 mAh cm^{-3}. The higher capacity of *NMC-500C* than *NMC-as-dep* supports the stabilization of the amorphous film during the annealing process. The difference in peak positions in the dQ/dV plot indicate the electrochemistry

Table 1. Thickness of the active material and the Pt layer to gain an understanding of how the material reacts during the annealing process. The thickness and porosity were determined from cross-sectional and top-down SEM scans, respectively. The O/M ratio was determined via ERD and the capacity was determined via electrochemical measurements.

	NMC as dep	*NMC 500C O_2*	*NMC 700C O_2*	*Li_2CO_3 NMC 700C O_2*	*Li_2CO_3 NMC 700C O_2 - fast*	*NMC TiW 700C O_2*	*Li_2CO_3 NMC TiW 700C O_2*	*Li_2CO_3 NMC TiW 700C O_2 - washed*
Active film thickness (nm)	125	125	110	110	115	125	120	130
Porosity (%)	0	0	21.2	12.6	24.8	10.6	0	0
Li/M	0.9	1	0.4	0.7	0.4	0.8	2.1	1.2
O/M	1.9	2.0	1.5	1.8	1.5	1.8	3.2	2.1
Capacity density (mAh/cm^3)	605	860	255	570	315	660	1120	655
Pt thickness (nm)	65	65	105	170	225	70	130	125

is different for both materials even though both are amorphous. Surprisingly, the charge–discharge properties of the annealed, crystalline film were worse; the discharge capacity of *NMC-700C* was only at 2.2 µAh cm^{-2} (or 250 mAh cm^{-3} for an estimated 20% film porosity, **Table 1**). The decrease in capacity cannot be explained only by the 20% porosity of the film (as estimated from SEM), but not surprising considering the drastic composition change in the ERD profile due to loss of active material into the substrate. Interestingly, the sample annealed at 500°C delivered a capacity close to that obtained for NMC811 powder, with a practical capacity of ≈965 mAh cm^{-3}.[23,25–30] To our knowledge, this is the first report of high-capacity amorphous Ni-rich NMC thin-films achieving about 65% of their theoretical capacity. We believe that this increased capacity may be attributed to alterations in the local environment of both the film and substrate during the annealing process. This suggests that a high annealing temperature may not be required to achieve high performing thin film NMC. Note that a high capacity for amorphous thin films is not uncommon, for example TiO_2, V_2O_5 and $FePO_4$.[31–33]

2.2. Compensation for the In-Diffusion of Active Material Into the Substrate

To obtain a crystalline film with the desired NMC stoichiometry, compensation for the in-diffusion of Li_2O from the active material into the Pt layer is needed. Indeed, a migration of Li and O into the Pt layer, likely in the form of Li_2O, was found with ERD and XRD. Therefore, to compensate for the loss of Li_2O into the substrate, a "sacrificial" Li_2CO_3 layer, of 185 nm was deposited on top of the as deposited NMC film (**Figure 3**a,d). Remember that the Li_2CO_3 that formed on the surface, due to a reaction between H_2O, CO_2 and the active material (extracting Li_2O) during air exposure, reacted again with underlying active material during the 700°C anneal. Hence, our hypothesis here is that the excess deposited Li_2CO_3 can react with the Li_2O deficient NMC, thereby compensating for the loss of active material in the substrate, i.e., equalizing in- and out-diffusion resulting in a stoichiometric film after annealing.

When this stack was annealed at 700°C, a notable change in the sample appearance was observed in the SEM images (Figure 3b,e). This film exhibited less porosity as compared to *NMC-700C*, indicating that the intention at least partly worked and most of the Li_2O that was lost into the Pt substrate had been successfully replaced by reaction with the Li_2CO_2 film on top. A most interesting feature observed was the substantial volume expansion of the Pt layer. Hence, much of the Li_2O coming from the excess Li_2CO_3 actually had diffused all the way through the active material and lost again into the substrate during the annealing step. ERD analysis (Figure 3g) confirms a large Li and O content in the substrate (Pt). As no Li_2CO_3 remained on the surface, from SEM and ERD, the excess supply was indeed exhausted. Yet, the ERD composition analysis shows a much larger plateau segment in the depth profile composition (as opposed to the sloped profile seen in *NMC-700C*) with near stoichiometric Li and O composition, yet somewhat lower than the as-deposited film, consistent with a slight net loss and some porosity in the films.

It was anticipated that annealing with faster ramp rates could alleviate this issue as the film would spend less time at elevated temperatures, thus reducing the needed amount of Li_2CO_3 excess. Therefore, samples were annealed at 700°C using a faster ramp rate of 5°C s^{-1} as opposed to the 10°C min^{-1} used previously. In contrast to the expectation, however, the porosity has increased significantly (becoming similar to that without excess Li_2CO_3 in Figure 1c) and a particular waviness was observed with hillocks in the micrometer range (see Figure 3c,f; and Figure S6, Supporting Information). This wrinkling effect can be attributed to a lattice mismatch between the substrate and the active film. The greater porosity compared to the film that underwent a slower anneal, would also suggest a depletion in active materials in this scenario. ERD analysis of this film showed a sloped profile (Figure 3h), similar to that of *NMC-700C*, and at least partly due to the porous nature of the film. However, for this sample, the O to TM ratio seems lower than in the other cases, indicating that some oxygen from the active material transition metal oxide is also lost into the Pt film. This suggest a solid-state redox reaction where M_2O_3 is reduced, and Pt is oxidized to PtO_2. The specifics of these reactions will be discussed below.

A comparison of the third galvanostatic charge–discharge cycle and its corresponding dQ/dV plot for the films that underwent Li_2CO_3 treatment are shown in Figure 3i,j, respectively. The electrochemical properties of the as deposited film were also added as a reference. The discharge capacity of *Li_2CO_3-NMC-700C* is about 5.5 µAh cm^{-2} (corresponding to ≈520 mAh cm^{-3} for an estimated 13% film porosity, Table 1). This capacity is a lot higher than that of *NMC-700C*, further supporting that the deposited Li_2CO_3 compensates for some of the loss of Li_2O from the NMC film through reaction with the Pt current collector during annealing, regaining some of the capacity. When the annealing

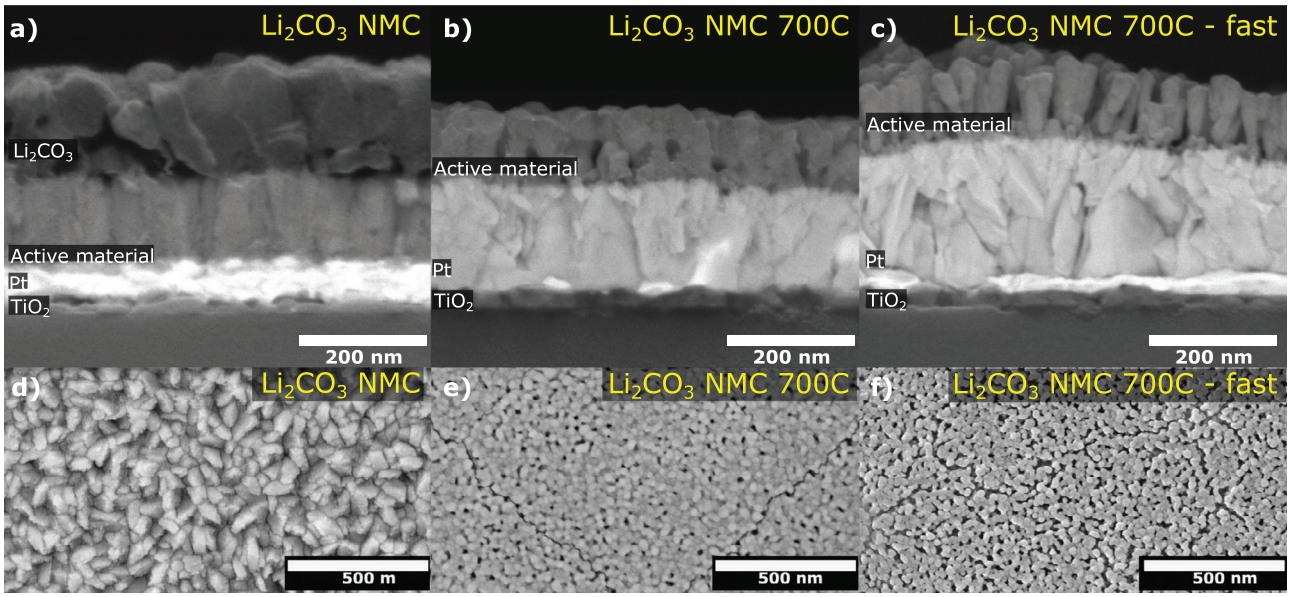

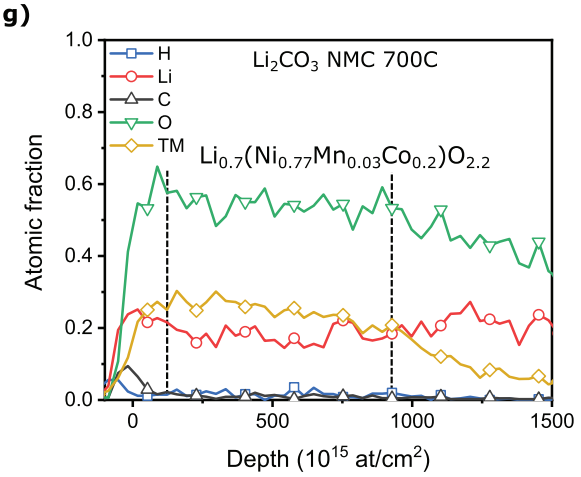

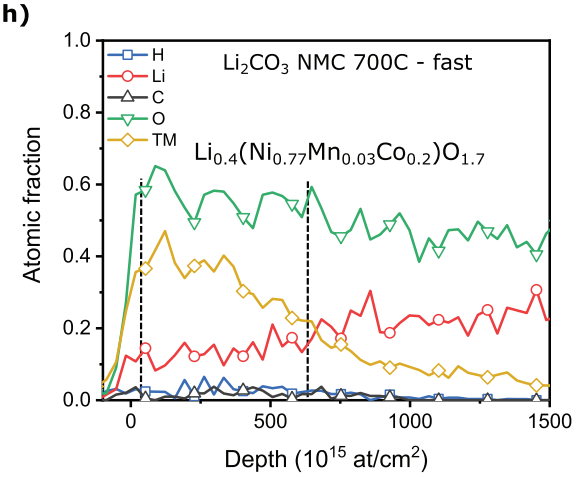

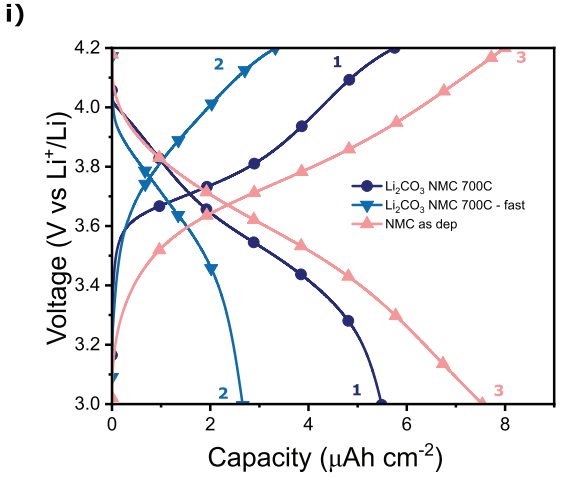

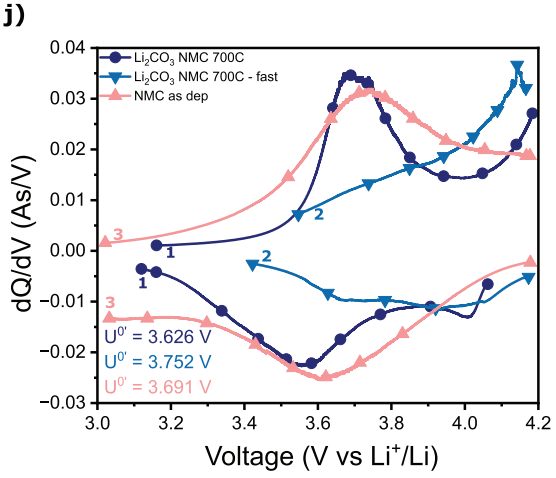

ramp rate was increased (*Li_2CO_3-NMC-700C-fast*), the capacity was halved to 2.7 μAh cm^{-2} (corresponding to about 340 mAh cm^{-3} for an estimated 25% film porosity, Table 1). However, the lithiation curve (toward more positive potentials) did not show a plateau anymore. Therefore, no peaks could be assigned in the dQ/dV scans, consistent with a change in active material composition. The results of the fast-annealing experiment indicate that next to Li_2O loss, another competing solid-state reaction is going on. Hence, despite having the Li_2CO_3 layer over the NMC prior to annealing, there was no significant benefit obtained when increasing the annealing rate, due to the transition metals also taking part in the reaction with Pt. Reducing one seems to benefit the other. Hence, control of exact NMC composition when in direct contact with Pt current collectors is difficult to achieve.

2.3. Utilizing a Diffusion Barrier to Block Reaction With Substrate

Another strategy that was implemented to minimize the diffusion of active material into the Pt layer was to introduce a thin diffusion barrier between the NMC and Pt layers. In the case of LNMO thin-films, indium-tin-oxide (ITO) was found to be a good diffusion barrier for loss of active material in the underlying Pt current collector.[34] For our Ni-rich films, 10 nm of ITO, as well as TiO_2 and TiW were evaluated for this purpose. While ITO and TiO_2 did not improve the capacity of the films as compared to *Li_2CO_3-NMC-700C*, the capacity of the films deposited on TiW more than doubled (comparison in Figure S7, Supporting Information). Therefore, we further investigated utilizing TiW as a diffusion barrier during annealing. Three conditions were explored; the first involved depositing NMC on 10nm TiW and annealing it at 700°C (*NMC-TiW-700C*). The second condition entailed depositing an additional Li_2CO_3 layer on top before annealing (*Li_2CO_3-NMC-TiW-700C*), and in the third case, the sample that underwent the previous condition was washed with methanol for 5 min after annealing (*Li_2CO_3-NMC-TiW-700C-washed*). This was done as alcohol has been used as a solvent to remove surface species on NMC cathodes.[35]

Figure 4a,d shows the cross-section and top down views of *NMC-TiW-700C*. Here the film maintains its columnar morphology as was seen in the as deposited film. The relative lack of porosity as compared to *NMC-700C* as well as the lack of volume expansion of the Pt layer suggests that the reactions that had previously occurred between film and substrate had largely been suppressed when a TiW interlayer is added. The ERD depth profiles indeed show nearly stoichiometric composition throughout the full film thickness (Figure 4g), showing that TiW reduced the diffusion of transition metal and also Li_2O. With a Li/TM ratio of 0.7 compared to 0.9 for the as-deposited films (Figure 1g), some Li_2O might still be lost through TiW. Some gaps were still observed between the NMC and TiW/Pt substrate, indicating the possibility of some material loss but it can also be the result of crystallization and grain growth during annealing. The addition of an excess Li_2CO_3 layer above the NMC prior to annealing now resulted in an excess of Li_2O after annealing, demonstrating that TiW is indeed a barrier also for Li_2O. A web-like layer was still present on the surface (Figure 4b,e). The depth scan of this sample (Figure 4h) showed that the film had a surface layer comprised of Li and O (likely Li_2O from the decomposition of Li_2CO_3). Moreover, the bulk of the film also appeared to be rich in Li and O which is believed to be Li_2O forming a nanocomposite with the NMC film. Note that the SEM shows larger grain size in the top-down view. Once the film is saturated with Li_2O, the excess remained on the surface. When the sample was washed with methanol the Li and O significantly decreased throughout the bulk of the film approaching closer to NMC stoichiometry (Figure 4i). The methanol treatment did not (yet) remove all Li_2O, leaving behind a large portion of the webbed top layer.

The electrochemical properties of these films are shown in Figure 4j, k. The discharge capacity of *NMC-TiW-700C* was about 7.33 μAh cm^{-2}, corresponding to ≈ 660 mAh cm^{-3} (for an estimated 11% porosity, see Table 1). This is the highest Li-ion capacity density of all the crystalline films so far (700°C samples) on Pt (i.e., without a TiW interlayer), even with Li_2CO_3 excess, further supporting that the reactions between film and substrate had been suppressed by the TiW barrier, and similar to that of the as deposited amorphous NMC film (605 mA cm^{-3}), but still lower than the 500°C annealed amorphous film (860 mA cm^{-3}). The reason for the lower capacity as compared to *NMC-500C* can still be explained by small amounts of material loss to the substrate, even though this is much less than that without the TiW layer. Surprisingly, the capacity of the Li_2O rich NMC film (*Li_2CO_3-NMC-TiW-700C*) was about 13.41 μAh cm^{-2}, corresponding to 1120 mAh cm^{-3}. This high electrochemical performance is attributed to the excess Li_2O in the film, resulting in a Li_2O-NMC solid nanocomposite. Finally, removal of the excess Li_2O by washing with methanol reduced the capacity again to about 9.23 μAh cm^{-2}, corresponding to 695 mAh cm^{-3}, i.e., similar to that of *NMC-TiW-700C*.

2.4. Role of Oxygen in the Annealing Atmosphere

To evaluate how the annealing atmosphere affects the reaction with Pt, we deposited Li_2CO_3 on a Pt substrate, as shown in **Figure** 5a. Subsequently, the film was annealed in both O_2 and

Figure 3. a–f) Cross-sectional and top-down SEM images of (a,d) Li_2CO_3 deposited onto NMC (*Li_2CO_3-NMC*). This sample was then either annealed (b,e) at 700°C at the same ramp rate used in previous experiments (*Li_2CO_3-NMC-700C*) or (c,f) annealed using a faster ramp rate of 5°C s^{-1} (*Li_2CO_3-NMC-700C-fast*). ERD depth scans of (g) *Li_2CO_3-NMC-700C* and (h) *Li_2CO_3-NMC-700C-fast*. An approximation of the composition was determined from the atomic fraction between the dashed lines. The Li content was still not completely compensated for when annealed with a Li_2CO_3 layer. Comparison of the voltage versus capacity and the corresponding dQ/dV plots of (i,j) *Li_2CO_3-NMC-700C* and *Li_2CO_3-NMC-700C-fast* during galvanostatic charge–discharge measurements. The electrochemical profile of the as-deposited sample was added as a reference. The charge discharge measurements were conducted after three cyclic voltammetry measurements at 1 mV s^{-1}. The figure depicts the 3rd charge–discharge scan. The charge–discharge measurements were performed at a current density of 0.349 μA cm^{-2}. The formal potentials ($U^{0'}$) of the third charge–discharge cycle of each film are indicated in the dQ/dV scans. The charge–discharge and dQ/dV curves are labeled 1, 2, and 3 to represent *Li_2CO_3-NMC-700C*, *Li_2CO_3-NMC-700C-fast* and *NMC-as-dep*, respectively.

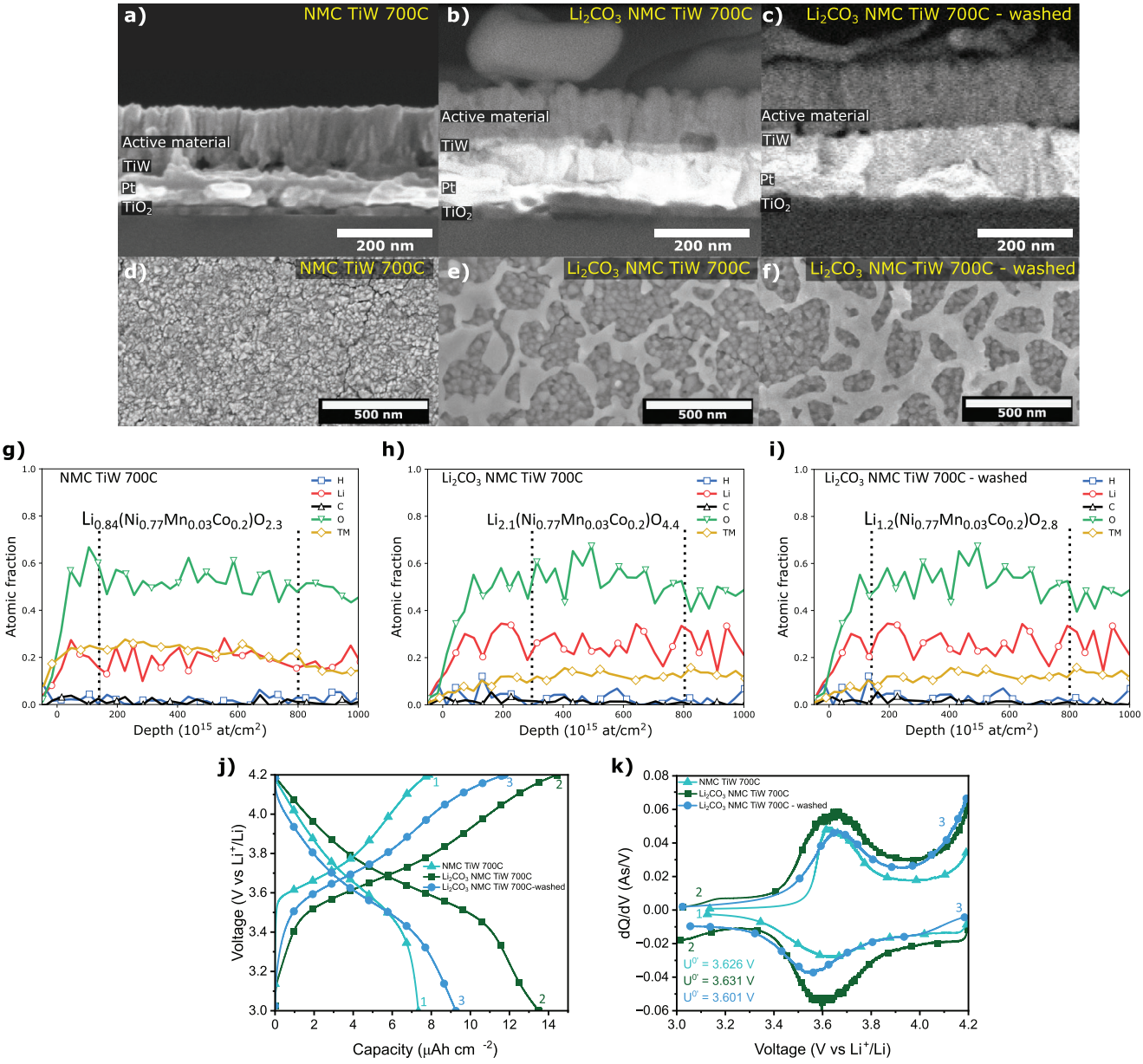

Figure 4. a–f) Cross-sectional and top-down SEM images of (a,d) NMC annealed with a TiW interlayer, without (*NMC-TiW-700C*) and with (*Li_2CO_3-NMC-TiW-700C*) a Li_2CO_3 surface layer. The previous sample was also washed with methanol for 5 min to remove the surface species (*Li_2CO_3-NMC-TiW-700C-washed*). ERD depth scans of (g) *NMC-TiW-700C*, h) *Li_2CO_3-NMC-TiW-700C* and (i) *Li_2CO_3-NMC-TiW-700C-washed*. An approximation of the composition was determined from the atomic fraction between the dashed lines. Comparison of the voltage versus capacity and the corresponding dQ/dV plots of (j,k) *NMC-TiW-700C*, *Li_2CO_3-NMC-TiW-700C*, and *Li_2CO_3-NMC-TiW-700C-washed* during constant current charge-discharge measurements. The charge–discharge measurements were conducted after three cyclic voltammetry measurements at 1 mV s^{-1}. The figure depicts the 3rd constant current charge–discharge scan. The charge–discharge measurements were performed at a current density of 0.349 μA cm^{-2}. The formal potentials ($U^{0'}$) of the third charge-discharge cycle of each film are indicated in the dQ/dV scans. The charge–discharge and dQ/dV curves are labeled 1, 2, and 3 to represent *NMC-TiW-700C*, *Li_2CO_3-NMC-TiW-700C* and *Li_2CO_3-NMC-TiW-700C-washed*, respectively.

Ar atmospheres, with the aim of determining whether, and under what specific conditions, a reaction between Li_2CO_3 and the Pt substrate would occur. Upon annealing the film in an O_2 atmosphere (Figure 5b) it was observed that the entire film was destroyed, reacting away the complete film and even into the underlying silica. In contrast, when annealing in an Ar atmosphere, as shown in Figure 5c, the Li_2CO_3 top layer had disappeared, and a uniform and continuous smooth film was obtained. Interestingly, in this case as well, the region below the Pt layer had changed, suggesting that the lithiated species (likely Li_2O) move through the dense reacted Pt layer, akin to a solid-state diffusion lead reaction front (as opposed to a direct reaction between the components as could be the case for Figure 5b). In the oxygen ambient, Pt can oxidize to PtO_2 which reacts further with

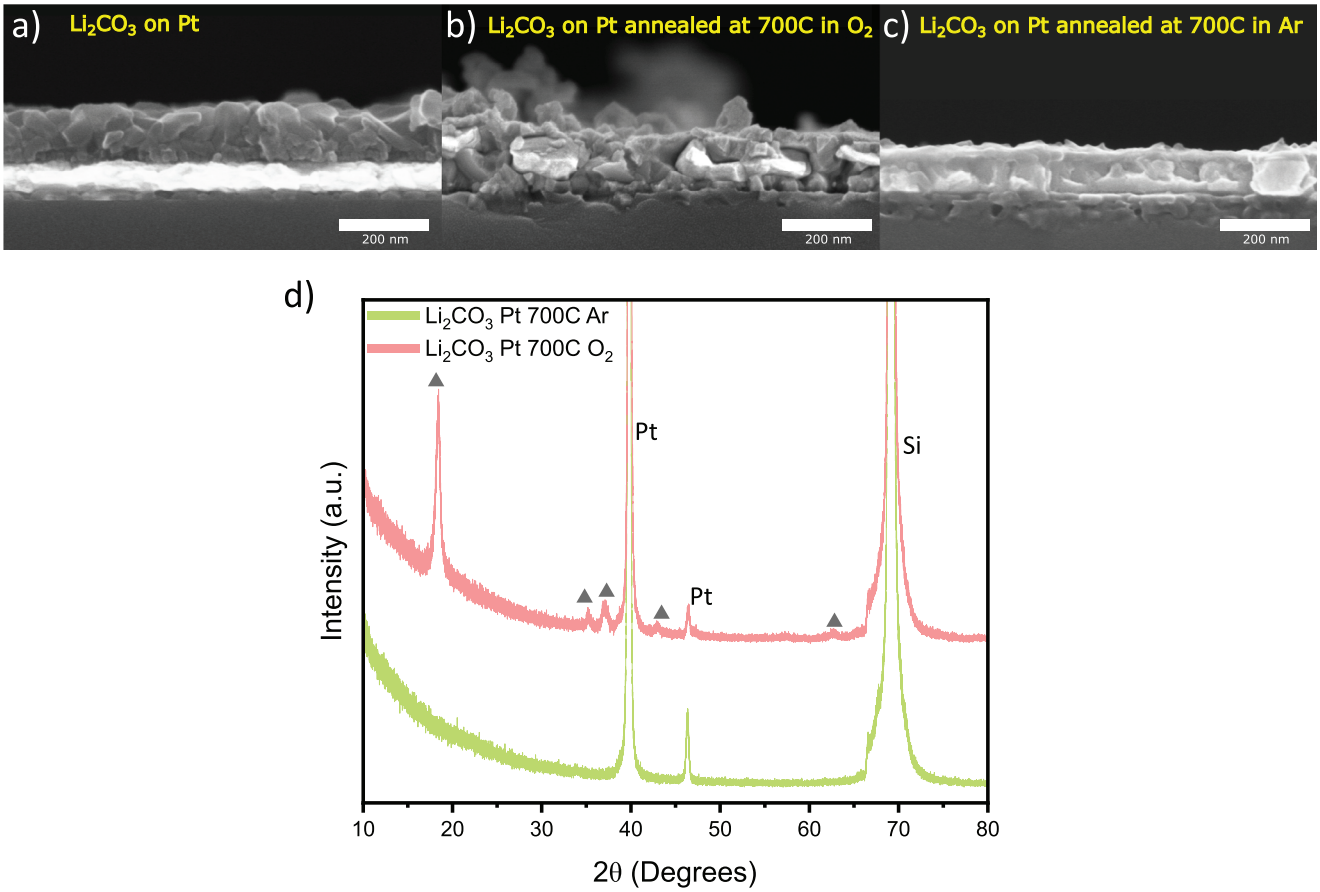

Figure 5. Cross-sectional SEM images of (a) Li_2CO_3 on a 70nmPt/ 10nmTiO_2/ 300nmSiO_2/ Si substrate prior to annealing. As well as this film annealed at 700°C in (b) O_2 and (c) Ar. The images have been aligned based on the TiO_2/Pt interface to show that the underlying SiO_2 also takes part in the reaction during annealing. d) 2theta-omega XRD scans of each film after annealing in either an O_2 or Ar atmosphere. Triangles indicate Li_2PtO_3 peaks.

Li_2CO_3 (or Li_2O) to form Li_2PtO_3 (more detail in next section). However, in the absence of O_2 (Ar environment of Figure 5c), in principle no or only limited amounts of PtO_2 will be available and this would imply that Li_2O must diffuse through the Pt film, reacting with TiO_2 and SiO_2. Hence Pt does not act as an effective Li_2O diffusion barrier. In fact, the Pt film in Figure 5c seems to have doubled in thickness, indicating that a Pt-Li_2O composite is formed. These observations are confirmed by XRD (Figure 5d). When annealed in Ar, only peaks relating to Pt and Si were observed, once again suggesting that Li_2O did not form a new compound with the Pt. However, the sample annealed in O_2 showed distinct XRD peaks for Li_2PtO_3 (denoted by a triangle in Figure 5d),[36] supporting our hypothesis that Li_2O reacts with Pt in the presence of O_2 to form Li_2PtO_3.

The annealing experiment with Li_2CO_3 on Pt in O_2 indeed explains the loss of Li_2O from the active material, observed above. When NMC is annealed in O_2 atmosphere, the oxygen still has access to the underlying Pt layer as the NMC has some porosity at all times: at first via the grain boundaries (see as-deposited film in Figure 1a) and eventually through pores resulting from loss of active materials (see Figure 1c). Hence, PtO_2 is formed on the Pt surface which then reacts further with the Li_2O from the NMC, forming Li_2PtO_3.

2.5. Understanding the Reaction Pathways During Annealing

Table 1 summarizes the results obtained for all the samples, comparing the thicknesses of the active material and Pt in each sample, as well as the discharge capacity density, porosity and O/M ratio of each film studied.

Figure 6 depicts the thickness results in a bar chart with the thickness of both, the active NMC material as well as the Pt current collector, for each of the conditions studied. The error bars indicate the variance of the SEM measured thicknesses over multiple samples. The thickness of the active NMC film as well as the Pt current collector was unchanged between the as deposited film and one annealed at 500°C, indicating that minimal, if any, interfacial reactions occur between the film and substrate during a 500°C anneal.

When annealed at 700°C in the presence of O_2, there is a noticeable decrease in the active material thickness together with increase in porosity (see below) and a subsequent increase in the Pt thickness, suggesting that during annealing at 700°C, active material moves from the NMC film into the Pt layer. When annealed with a Li_2CO_3 layer on top, an additional notable increase of the Pt layer was found, with Li_2CO_3 layer being a larger Li_2O source. A faster ramp rate resulted in a varying thickness

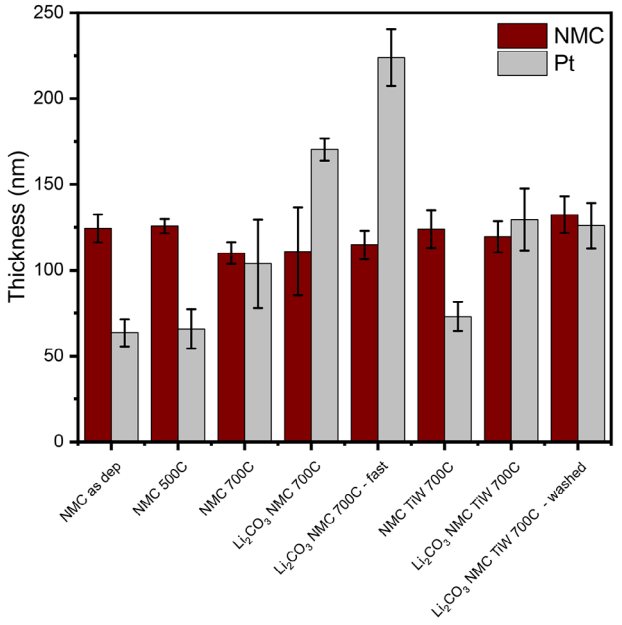

Figure 6. Comparison of the thickness of the NMC active material and the Pt layer between samples. These values were taken from the results shown on Table 1 The NMC as dep sample was used as a reference and was determined via cross sections from six different as deposited samples. The change in thickness between each sample offers insight into the movement of species during the annealing process. The error bars represent the standard deviation in each measurement.

profile with on average a thicker Pt film again suggesting that the reaction between NMC, Li_2O and Pt has competing kinetic components. This film was also more inhomogeneous, with a greater porosity, potentially due to an amplification of any lattice strain between the film and substrate. Finally, a TiW interlayer was introduced as a diffusion barrier between the NMC and Pt layers. This resulted in no change in thickness for both NMC and Pt suggesting that the reaction between the active material and the Pt substrate was at least severely suppressed. When the TiW diffusion barrier was utilized together with a Li_2O excess layer (in the form of Li_2CO_3), the Pt film thickness increased again. However, the SEM and ERD analysis clearly showed that the NMC layers were supersaturated with Li_2O, forming an NMC-Li_2O composite, again advocating the good barrier properties of TiW. Therefore, we believe that the measured increase in Pt thickness (which is markedly less than that without TiW) is the result of leakage of Li_2O through the TiW likely via grain boundaries and cracks.

Next, we will explain these results with a set of solid-state and solid-gas reactions given in **Table 2**. As the reactions occur mostly during the annealing process, their Gibbs free energy is given at 500 and 700°C.

ERD and XRD showed the formation of a Li_2PtO_3 phase in case of annealing in oxygen and with active material in direct contact with Pt. The Pt layer acts as a Li_2O sink during the annealing process where the Li_2O comes from the active material and supply is maintained when an excess Li_2CO_3 is placed on top of the NMC film. However, the reaction between Li_2O and Pt to form Li_2PtO_3 would only occur when Pt is in its oxidized form (PtO_2). As annealing was performed in an O_2 atmosphere, the Pt can react with the O_2 and form PtO_2, which can then react with Li_2O via reactions 1 and 2. From these reactions, it follows that while only a fraction of PtO_2 can form during annealing of Pt in oxygen (reaction 1 is non-spontaneous). It will spontaneously react with Li_2O to form Li_2PtO_3, shifting the total equilibrium to the right (as seen in Equation (3)) i.e., the reaction with Pt can go to completion forming Li_2PtO_3 in the presence of O_2 and sufficient O^{2-} and Li^+ sources.

When an NMC film is present on top of the Pt substrate, O_2 could still reach the Pt via pores in the active film and by diffusion along the film grain boundaries leading to reaction three during annealing in an oxygen atmosphere. However, as the O/M ratio decreased at 700°C for NMC films in direct contact with Pt, the transition metals likely also react with Pt during annealing. NMC can be described as a solid solution of $LiNiO_2$, $LiCoO_2$, and $LiMnO_2$, in our case about 80% of $LiNiO_2$. These lithiated compounds can decompose into Li_2O and the transition metal oxides according to Equations (4)–(6). For the reactive $LiNiO_2$, decomposition into Li_2O and Ni_2O_3 would be already thermodynamically favorable at 700°C. The Ni_2O_3 can now oxidize Pt to PtO_2 while being reduced to NiO in the process (reaction 7). Also, the combination of Equations (2), (4), and (7) is favorable and thus Pt can react directly with the NMC film to form NiO and Li_2PtO_3 (Equation (13)). While the reaction between Ni_2O_3 and the substrate are spontaneous, similar reactions with Co_2O_3 and Mn_2O_3 are not, as seen in Equations (14) and (15). Hence, the reactivity of NMC is due to the reactive $LiNiO_2$ fraction. Interestingly, the ERD profiles show that O/M ratio changes quite far into the film. Hence, the reaction between NMC ($LiNiO_2$) and Pt is likely not limited to the interface and NiO diffuses into the film and $LiNiO_2$ to the surface, most likely by concentration driven galvanic exchange:

$$NiO_{(s),site1} + LiNiO_{2(s),site2} = LiNiO_{2(s),site1} + NiO_{(s),site2} \quad (17)$$

Also, the loss of Li_2O into the Pt with (concurrent) formation of Li_2PtO_3 contributes to the O/M ratio change. Whereas the ΔG for reaction 14 is negative both at 500 and 700°C. The striking difference in ERD profiles indicates much faster diffusion of both NiO/$LiNiO_2$ and Li_2O/Li_2PtO_3 for the higher temperatures. Note that the change in surface morphology, i.e., becoming more porous as a result of loss of active material, also allows easier access of O_2 to the Pt substrate, accelerating reaction 2. The uptake of Li_2O and formation of Li_2PtO_3 is apparent from the thickness change in Figure 6. The fast ramp rate experiment (with excess Li_2CO_3) highlighted the effect of the different reaction/diffusion kinetics for competing reactions in combination with variations in the morphology.

To determine in which conditions the transition metals oxidize Pt, the O/M ratio was determined for each sample. This was done after subtracting the O required to form Li_2O in Equations (4)–(6) from the total O content in the sample. If the transition metals do not react with Pt, the O/M ratio will remain constant. However, if they do oxidize the Pt layer, the O/M ratio will decrease.

The Li/M and O/M (after Li_2O subtraction) ratios are plotted against the porosity of each film (**Figure 7**) to determine whether the porosity is correlated to the reaction of Li_2O and transition metal oxides with the Pt. From this plot, there is a trend that as the Li/M and O/M ratios decreases due to reaction with Pt, the degree of porosity increases. For *NMC-as-dep* and *NMC-500C*

Table 2. Potential reactions that occur during the annealing process, along with their Gibbs free energy at 500 and 700°C. The Gibbs free energies were calculated with the HSC Chemistry nine software.

Reaction		$\Delta G_{500°C}$ (kJ mol^{-1})	$\Delta G_{700°C}$ (kJ mol^{-1})
$Pt_{(s)} + O_{2(g)} \rightleftharpoons PtO_{2(l)}$	(1)	0.32	28.17
$Li_2O_{(s)} + PtO_{2(l)} \rightleftharpoons Li_2PtO_{3(s)}$	(2)	−67.38	−58.28
$Pt_{(s)} + Li_2O_{(s)} + O_{2(g)} \rightleftharpoons Li_2PtO_{3(s)}$	(3)	−67.06	−30.11
$2LiNiO_{2(s)} \rightleftharpoons Li_2O_{(s)} + Ni_2O_{3(s)}$	(4)	1.56	−19.98
$2LiCoO_{2(s)} \rightleftharpoons Li_2O_{(s)} + Co_2O_{3(s)}$	(5)	151.72	143.29
$2LiMnO_{2(s)} \rightleftharpoons Li_2O_{(s)} + Mn_2O_{3(s)}$	(6)	147.68	151.25
$2Ni_2O_3 + Pt_{(s)} \rightleftharpoons PtO_{2(l)} + 4NiO_{(s)}$	(7)	−114.39	−127.49
$2Co_2O_{3(s)} + Pt_{(s)} \rightleftharpoons PtO_{2(l)} + 4CoO_{(s)}$	(8)	33.57	16.91
$2Mn_2O_{3(s)} + Pt_{(s)} \rightleftharpoons PtO_{2(l)} + 4MnO_{(s)}$	(9)	205.94	190.41
$Ni_2O_3 + Pt_{(s)} \rightleftharpoons PtO + 2NiO_{(s)}$	(10)	−62.58	24.11
$Co_2O_{3(s)} + Pt_{(s)} \rightleftharpoons PtO + 2CoO_{(s)}$	(11)	11.40	4.74
$Mn_2O_{3(s)} + Pt_{(s)} \rightleftharpoons PtO + 2MnO_{(s)}$	(12)	97.59	91.49
$2LiNiO_{2(s)} + Ni_2O_{3(s)} + Pt_{(s)} \rightleftharpoons Li_2PtO_{3(s)} + 4NiO_{(s)}$	(13)	−180.21	−205.75
$2LiCoO_{2(s)} + Co_2O_{3(s)} + Pt_{(s)} \rightleftharpoons Li_2PtO_{3(s)} + 4CoO_{(s)}$	(14)	117.91	101.92
$2LiMnO_{2(s)} + Mn_2O_{3(s)} + Pt_{(s)} \rightleftharpoons Li_2PtO_{3(s)} + 4MnO_{(s)}$	(15)	286.24	283.38
$Li_2CO_{3(s)} \rightleftharpoons Li_2O_{(s)} + CO_{2(g)}$	(16)	103.36	75.62

the porosities were both zero as no significant material reacted with the substrate. The O:M ratio was 1.9 and 2.0 for *NMC-as-dep* and *NMC-500C*, respectively (Table 1). The porosity increased to 21.2% for *NMC-700C*, which was also combined with a decrease in the O:M ratio to 1.5. This trend continues for all the samples measured, with the exception of the *Li_2CO_3-NMC-700C-TiW* film. This film had zero porosity, which may be due to the Li_2CO_3 surface layer not being completely removed after annealing. The O/M ratio for this film was extremely high, at 3.2, once again suggesting that the Li_2O formed a composite with the NMC instead of a lithiated compound.

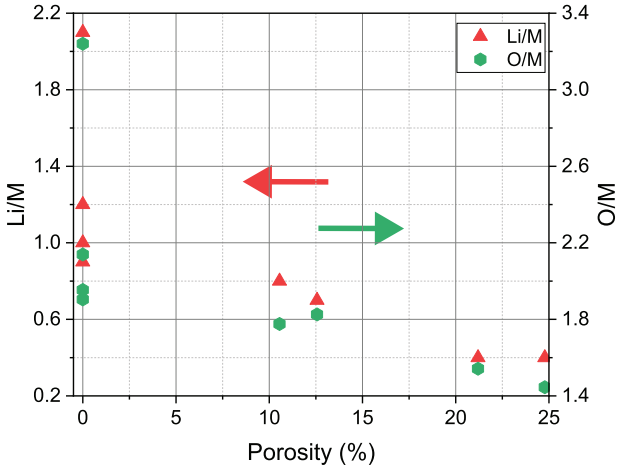

Figure 7. Plot of the Li/M (left) and O/M (right) ratio versus the porosity of the film. The data points are based on values from Table 1.

The movement of Li_2O from the NMC layer to the Pt layer was compensated for by depositing a Li_2CO_3 layer on the NMC prior to annealing. During annealing Li_2CO_3 decomposed into Li_2O and CO_2 via reaction 16. This reaction is not spontaneous, however, as CO_2 is being purged from the annealing chamber, the equilibrium shifts to the right, further decomposing Li_2CO_3. This leaves Li_2O behind, allowing for it to react with the Li_2O depleted NMC on the surface, reforming NMC.

2.6. Assessment of NMC Quality from Electrochemical Parameters

Figure 8 compares the formal potential of each of the films analyzed in this study. The formal potential was determined from the average of the anodic and cathodic peaks.[37,38] The horizontal dashed lines are where the formal potentials are found in NMC composite cathodes, based on literature.[6] These formal potentials in Ni-rich NMC are generally attributed to various phase transitions. These phase transitions are commonly denoted as H1 to M, M to H2 and H2 to H3. The individual phases are named by their symmetry (H: hexagonal and M: monoclinic) and their order of appearance during delithiation.[1,39,40] Charge–discharge profiles of our films show dQ/dV peak positions between 3.6 and 3.75V, i.e., closest to the H1 to M transition

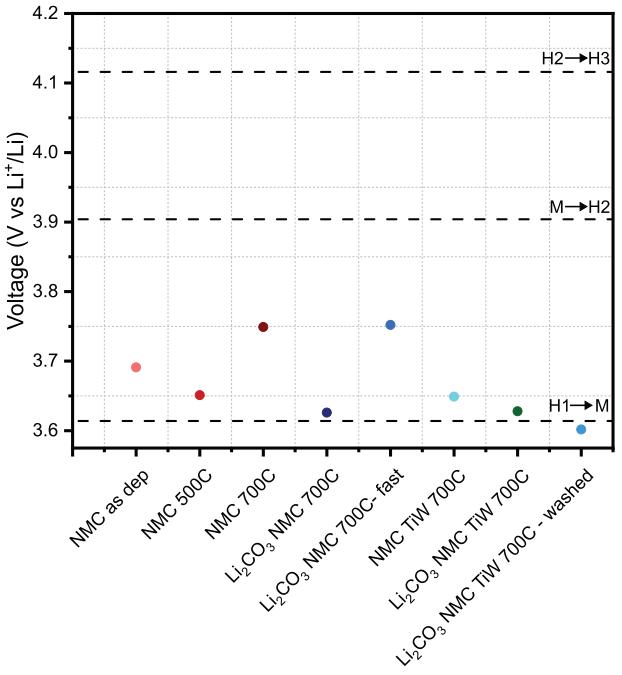

Figure 8. Comparison of the formal potential of each of the samples studied. The formal potential was derived from the average of the anodic and cathodic peaks from the dQ/dV scan. The formal potential was taken at the 3rd charge–discharge cycle, allowing the film to stabilize. The horizontal dashed lines at 3.61, 3.90, and 4.12 V depicts the expected formal potentials for Ni-rich NMC.[6]

observed in bulk NMC systems. The lack of higher phase transitions in the thin film system could be an advantage as some of these transitions, especially the H2 to H3, are known to degrade the cathode during electrochemical cycling. Nevertheless, the formal potentials can still be compared to that of literature to gain an insight into the purity of each film, considering the O/M ratio.

The amorphous *NMC-as-dep* film displays a formal potential of 3.69 V, i.e., about 75mV higher than what is expected for crystalline bulk material. For the amorphous yet activated film annealed at 500°C, the formal potential of 3.65 V is only 35 mV different to that of crystalline bulk material. Conversely, if the film is further heated to its crystalline temperature, 700°C, the formal potential of 3.75 V deviates with more than 130 mV from the expected behavior. As the average Li/M and O/M ratios decrease, there is an increased amount of transition metal oxides in the film, explaining the shift in formal potential. The formal potential of the *Li_2CO_3-NMC-700C* film, at 3.63 V, was again closer to what is expected for NMC. This is due to the film partially regaining its initial stoichiometry from the excess Li_2CO_3 layer. However, this is only the case when annealed with a relatively slow rate. When a faster rate was utilized, the formal potential was similar to *NMC-700C*, at 3.75 V. This change can also be seen by the Li/M and O/M ratios, as these ratios increase for *Li_2CO_3-NMC-700C* and decrease again for *Li_2CO_3-NMC-700C-fast*, signifying a deviation from the expected NMC composition. The formal potentials for the films that had a TiW diffusion beneath the NMC layer were all similar to that expected for NMC, which is in line with their constant stoichiometry and high electrochemical performance.

3. Conclusion

Thin-film NMC electrodes were prepared for the use as a model system, allowing for a detailed analysis of the interfacial reactions without the influence of passive components that are present in commercial cathodes. Amorphous NMC films were deposited onto a Pt substrate via RF sputtering. Surprisingly, this film demonstrated some electrochemical behavior after an activation charge, which is not generally seen in amorphous NMC cathodes. However, this film was also quite unstable and reacted spontaneously with air to form a Li_2CO_3 layer on the surface. Annealing the film at 500°C was found to partially activate the film and resulted in a significant capacity increase. This film was still amorphous, indicating that crystallization may not be necessary to fabricate a high-performing NMC film. Therefore, this can allow for the utilization of lower temperatures during NMC preparation, which reduces the overall cost. To crystallize the film, annealing at 700°C in an O_2 atmosphere, was required. After the anneal, all the Li_2CO_3 on the surface was removed and reacted back into the film. However, there was also a significant loss in Li and O with the film, leading to a porous film with a poor electrochemical performance. In conjunction with this, the thickness of the Pt substrate was found to increase after annealing, indicating a net movement of active materials, in the form of Li_2O and Ni_2O_3, from the film to the substrate. Depositing an excess Li_2CO_3 layer above the NMC film before annealing can help partially compensate for the reaction between NMC and Pt. However, this does not compensate fully, as the reaction rate between NMC and Pt is likely faster than that between Li_2CO_3 and NMC. Also, the excess Li_2CO_3 will not compensate for reactions between Ni_2O_3 and Pt. The use of a thin TiW diffusion barrier helped slow the reaction rate between NMC and Pt during annealing, resulting in a stoichiometric NMC composition, similar to that of an as deposited sample. The electrochemical behavior also resembled that expected of NMC materials. Therefore, a TiW diffusion barrier can be used to achieve a high performing crystalline NMC film. The reaction pathways explored in this article, along with the strategies proposed to mitigate the undesired reactions, can be used in the fabrication of thin-film NMC cathodes. It should also be noted that Pt is a noble metal, so if NMC oxidizes it at high temperatures, it likely also reacts with other materials present in the electrode during battery operation. For example, the reaction between Li_2O, Ni_2O_3 and C to form Li_2CO_3 and NiO is spontaneous at room temperature and the elevated temperatures during battery operation may assist in crossing the activation energy barrier. As carbon is present in various components of a battery, such as the conductive additive, in the polymeric binder and in the electrolyte solution, it likely reacts with the active NMC material to form Li_2CO_3. Therefore, attention must be paid to reduce these reactions during battery operation.

4. Experimental Section

Thin-Film Fabrication: NMC thin films were deposited onto a 70nmPt/10nmTiO_2/300nmSiO_2 substrate via RF magnetron sputtering. This involved the use of a Kurt J. Lesker sputtering tool that was connected to an Ar-filled glovebox. A three-inch NMC811 sputtering target, supplied by Neyco, was utilized in the process. Plasma ignition was achieved with a power of 30 W, using an Ar flow at a pressure of 10 mTorr. Subsequently,

Table 3. Conditions that were investigated as well as their approximate exposure times to ambient air before being analyzed. Due to the high temperature oven's location outside the glovebox, the samples annealed at 700°C were exposed to air for approximately 30 min longer than the other two samples (owing to 15 min of transportation to and from the oven). There was also an increase in the sample's exposure time prior to ERD and SEM measurements in comparison to electrochemical measurements. This disparity can be attributed to the location of the potentiostats within a glovebox, allowing the samples to be transported to the instrument without being exposed to ambient atmosphere. Conversely, the ERD and SEM tools were situated outside the glovebox, necessitating the removal of samples from the glovebox before being loaded into the tool. Given the inability to ascertain the exact duration of sample exposure, we opted to estimate an upper limit of 30 min to load each sample into the tool.

Sample	Condition	Exposure time before electrochemical measurements	Exposure time before ERD and SEM measurements
NMC-as-dep	As deposited sample without an annealing step	0 minutes	~30 minutes
NMC-500C	Annealed at 500°C in O_2 for 1 h at a ramp rate of 10°C min^{-1}	0 minutes	~30 minutes
NMC-700C	Annealed at 700°C in O_2 for 10 mins at a ramp rate of 10°C min^{-1}	~30 minutes	~1 hour
Li_2CO_3-NMC-700C	Li_2CO_3 deposited on NMC and annealed at 700°C for 10 mins at a ramp rate of 10°C min^{-1}	~30 minutes	~1 hour
Li_2CO_3-NMC-700C-fast	Li_2CO_3 deposited on NMC and annealed at 700°C in O_2 for 10 mins at a fast (5°C s^{-1}) ramp rate	~30 minutes	~hour
NMC-TiW-700C	NMC deposited on a 10 nm TiW diffusion barrier and annealed at 700°C for 10 mins at a ramp rate of 10°C min^{-1}	~30 minutes	~1 hour
Li_2CO_3-NMC-TiW-700C	NMC deposited on a 10 nm TiW diffusion barrier. Li_2CO_3 was deposited on top and annealed at 700°C for 10 mins at a ramp rate of 10°C min^{-1}	~30 minutes	~1 hour
Li_2CO_3-NMC-TiW-700C-washed	NMC deposited on a 10 nm TiW diffusion barrier. Li_2CO_3 was deposited on top and annealed at 700°C for 10 mins at a ramp rate of 10°C min^{-1}	~30 minutes	~1 hour

the power was ramped up to the deposition power of 55 W at a rate of 0.033 W s^{-1} and the pressure was decreased to 3 mTorr. A pre-sputtering procedure was performed for 10 min before exposing the substrate to the plasma. This was done in order to eliminate any impurities that may have been present on the target surface. Following the deposition, the samples were stored in an argon-filled glovebox. A 2-h deposition was performed to achieve a film thickness of 125 nm.

The samples were annealed in an O_2 atmosphere to counter the decomposition of NMC due to loss of oxygen and reduction of Ni^{+3} to form a NiO rock salt structure.[23]

The impact of temperature on the characteristics of the sample was investigated by analyzing films that underwent annealing at temperatures both at and below the crystalline temperature. Annealing at 700°C required the samples to be taken out of the glovebox to be transferred to the oven. The standard 700°C anneals were performed in a Nabertherm tube furnace with pure oxygen purging through at atmospheric pressure. An annealing temperature of 500°C was utilized for *NMC-500C* and was performed in the deposition tool itself, preventing exposure of the sample to air. The deposition tool was not capable of annealing at 700°C, therefore the Nabertherm tube furnace was utilized for this process.

Atomic layer deposition was used to deposit Li_2CO_3 onto the NMC surface. Lithium tert-butoxide (Li*O*t*Bu*) was used as the lithium source. This was combined with H_2O and CO_2 as co-reactants to eventually form Li_2CO_3. The reactor temperature during deposition was 250°C. Li*O*t*Bu* was pulsed for 5 s and was followed by a purging step of 15 s. H_2O and CO_2 had pulse/purge times of 0.5/15 s and 7.5/5 s, respectively.

The preparation conditions of each sample studied, as well as the approximate times they were exposed to ambient air before measurement, are outlined in **Table 3**.

Chemical Composition: The film composition was determined using a combination of three analytical techniques, namely, Elastic Recoil Detection analysis (ERD), Energy Dispersive X-Ray (EDX), and X-ray photoelectron spectroscopy (XPS). XPS was specifically employed to investigate the uppermost surface of the film, utilizing a PHI – VersaProbe III Scanning XPS Microprobe equipped with an Al source. In the ERD experiments, primary ion beams of I^{7+} or Br^{+5} were employed, accelerated to 13.628 or 10.01 MeV, respectively, by a 2 MV tandem accelerator. The forward recoiled and scattered ions were detected with a Time of flight - Energy (ToF-E) telescope. The telescope had a length of 755.4 mm and was installed at a forward scattering angle of 40°. While ERD did not give the absolute values of elements present in a film, it provided the atomic concentration of each element within the film, allowing for a ratio between these elements to be determined. ERD was primarily suited to detect the lighter elements (atomic number <14) in a thin film sample. Although the detection of heavier entities was possible, the technique's ability to distinguish between heavy elements with similar atomic weights was limited.

This sensitive nature of ERD toward lighter elements was taken advantage of to determine the Li:TM:O ratio. However, the inability of ERD to distinguish between each TM (Ni, Co, and Mn) necessitated the use of EDX for determining the quantity of each TM present in the film. EDX was performed on the sample cross-section via a Titan G2 using an acceleration voltage of 200 kV.

X-Ray Diffraction: The crystallization temperature was determined via in situ XRD measurements using a Bruker D8 Discover XRD system equipped with a Cu X-ray source (λ = 1.5406 Å) and a linear X-ray detector. Additionally, ex-situ XRD was preformed over a broader 2θ range using a Malvern Panalytical X'pert diffractometer equipped with a Cu X-ray source and a PIXcel1D detector. As the samples were extremely thin (roughly 120 nm), grazing incidence XRD was also preformed using this set up to minimize any substrate effects. The samples were mounted on a Si wafer to avoid any interference peaks from the diffractometer sample holder.

Scanning Electron Microscopy: The surface morphology of the thin films was characterized using a Helios460 and a Verios scanning electron microscope (SEM). The thickness of the films was estimated via the sample's cross-section. This was done by taking the average of multiple points across 2–7 samples for each condition investigated. To mitigate the effects of charging during imaging, a layer of approximately 0.5 nm of Pt was deposited onto the surface of the film.

Electrochemical Measurements: Electrochemical measurements were preformed using a custom-made three electrode TeflonTM cell. The cell was clamped onto the substrate and filled with an excess liquid electrolyte (around 10 mL), with an O-ring (with an exposed surface area of 0.63 cm^2) in between to prevent electrolyte leakage. Electrical contact was established by contacting the substrate to a copper foil via the utilization of silver paste. Li metal was used as the counter and reference electrodes. All experiments were performed at room temperature using a $LiClO_4$ in propylene carbonate (PC) electrolyte solution. For ease of preparation, an ampule containing $LiClO_4$ (10 g, battery grade, dry, 99.99%, Sigma–Aldrich) was dissolved in propylene carbonate (100 mL, 99.7%, Sigma–Aldrich), resulting in a 0.94 M solution. Measurements were conducted in an Ar filled glove box. The electrochemical cells were controlled through a PGSTAT101 Autolab (Metrohm) potentiostat/galvanostat, using the Metrohm Nova 2.4 software. Cyclic voltammetry was performed within the range of 3 and 4.1 V vs Li^+/Li. Constant current lithiation and delithiation experiments were performed with a charging rate (C-rate) of 0.2 C (0.317 μA cm^{-2}). The calculated C-rate was based on the theoretical capacity of NMC.

Gibbs Energy Calculations: The Gibbs free energies of the reactions occurring during annealing were calculated using the HSC Chemistry nine software. For species where the Gibbs free energy was not known, they were approximated using the H, S, Cp, Estimates Module. This module gives an estimate of the entropy, enthalpy and heat capacity for a chemical species, allowing for the calculation of the Gibbs free energy. The estimation was based on statistical data mining methods, using stoichiometric element amounts, their oxidation states and interactions. These parameters were calculated automatically from the chemical formula. This approach, while not perfect, could provide a good first approximation on the potential reaction pathways.

Supporting Information

Supporting Information is available from the Wiley Online Library or from the author.

Acknowledgements

The authors thank Praveen Dara and Karim Alexandros Kantre for the execution and analysis of the ERD measurements. The authors thank Davy Deduytsche and professor Christophe Detavernier from UGent for performing in situ XRD measurements. Finally, the authors thank Kurt J. Lesker Company for supplying the Mini SPECTROS and Nano 36 glovebox cluster tool.

Conflict of Interest

The authors declare no conflict of interest.

Data Availability Statement

The data that support the findings of this study are available from the corresponding author upon reasonable request.

Keywords

diffusion, electrochemistry, Li-ion batteries, NiO, NMC, thin-film

Received: November 15, 2024
Revised: February 21, 2025
Published online: May 19, 2025

[1] H.-J. Noh, S. Youn, C. S. Yoon, Y.-K. Sun, *J. Power Sources* **2013**, *233*, 121.
[2] S.-M. Bak, E. Hu, Y. Zhou, X. Yu, S. D. Senanayake, S.-J. Cho, K.-B. Kim, K. Y. Chung, X.-Q. Yang, K.-W. Nam, *ACS Appl. Mater. Interfaces* **2014**, *6*, 22594.
[3] I. A. Shkrob, J. A. Gilbert, P. J. Phillips, R. Klie, R. T. Haasch, J. Bareño, D. P. Abraham, *J. Electrochem. Soc.* **2017**, *164*, A1489.
[4] K. Shizuka, C. Kiyohara, K. Shima, Y. Takeda, *J. Power Sources* **2007**, *166*, 233.
[5] R. Jung, R. Morasch, P. Karayaylali, K. Phillips, F. Maglia, C. Stinner, Y. Shao-Horn, H. A. Gasteiger, *J. Electrochem. Soc.* **2018**, *165*, A132.
[6] R. Jung, M. Metzger, F. Maglia, C. Stinner, H. A. Gasteiger, *J. Electrochem. Soc.* **2017**, *18*.
[7] N. V. Faenza, L. Bruce, Z. W. Lebens-Higgins, I. Plitz, N. Pereira, L. F. J. Piper, G. G. Amatucci, *J. Electrochem. Soc.* **2017**, *164*, A3727.
[8] M. Bichon, D. Sotta, E. De Vito, W. Porcher, B. Lestriez, *J. Power Sources* **2021**, *483*, 229097.
[9] M. Wood, J. Li, R. E. Ruther, Z. Du, E. C. Self, H. M. Meyer, C. Daniel, I. Belharouak, D. L. Wood, *Energy Storage Mater.* **2020**, *24*, 188.
[10] P. Oh, M. Ko, S. Myeong, Y. Kim, J. Cho, *Adv. Energy Mater.* **2014**, *4*, 1400631.
[11] F. Lin, I. M. Markus, D. Nordlund, T.-C. Weng, M. D. Asta, H. L. Xin, M. M. Doeff, *Nat. Commun.* **2014**, *5*, 3529.
[12] S.-K. Jung, H. Gwon, J. Hong, K.-Y. Park, D.-H. Seo, H. Kim, J. Hyun, W. Yang, K. Kang, *Adv. Energy Mater.* **2014**, *4*, 1300787.
[13] M. Abe, K. Suzuki, H. Minamishima, K. Kim, S. Taminato, M. Hirayama, R. Kanno, *J. Japan Soc. Powder Powder Metall.* **2015**, *62*, 531.
[14] G. Cherkashinin, M. Motzko, N. Schulz, T. Späth, W. Jaegermann, *Chem. Mater.* **2015**, *27*, 2875.
[15] K. Nishio, N. Nakamura, K. Horiba, M. Kitamura, H. Kumigashira, R. Shimizu, T. Hitosugi, *ACS Appl. Energy Mater.* **2020**, *3*, 6416.
[16] N. D. Phillip, R. E. Ruther, G. M. Veith, *ACS Appl. Energy Mater.* **2019**, *2*, 1405.
[17] H. Yim, W. Y. Kong, Y. C. Kim, S.-J. Yoon, J.-W. Choi, *J. Solid State Chem.* **2012**, *196*, 288.
[18] B. Yan, J. Liu, B. Song, P. Xiao, L. Lu, *Sci. Rep.* **2013**, *3*, 3332.
[19] G. Tan, F. Wu, J. Lu, R. Chen, L. Li, K. Amine, *Nanoscale* **2014**, *6*, 10611.
[20] M. Hirayama, M. Abe, S. Taminato, Y. Araki, K. Suzuki, R. Kanno, *RSC Adv.* **2016**, *6*, 78963.

[21] A. Aribia, J. Sastre, X. Chen, M. H. Futscher, M. Rumpel, A. Priebe, M. Döbeli, N. Osenciat, A. N. Tiwari, Y. E. Romanyuk, *Adv. Energy Mater.* **2022**, *12*, 2201750.
[22] V. Pimenta, M. Sathiya, D. Batuk, A. M. Abakumov, D. Giaume, S. Cassaignon, D. Larcher, J.-M. Tarascon, *Chem. Mater.* **2017**, *29*, 9923.
[23] J.-H. Shim, C.-Y. Kim, S.-W. Cho, A. Missiul, J.-K. Kim, Y. J. Ahn, S. Lee, *Electrochim. Acta* **2014**, *138*, 15.
[24] X. Cai, P. Yan, T. Xie, Y. Wu, C. Zheng, R. Shang, S. Yin, Y. Zhang, F. Zheng, X. Liu, J. Xie, *Adv. Funct. Mater.* **2024**, https://doi.org/10.1002/adfm.202423888.
[25] K. K. Cheralathan, N. Y. Kang, H. S. Park, Y. J. Lee, W. C. Choi, Y. S. Ko, Y.-K. Park, *J. Power Sources* **2010**, *195*, 1486.
[26] S. H. Ju, Y. C. Kang, *Ceram. Int.* **2009**, *35*, 1633.
[27] M.-H. Kim, H.-S. Shin, D. Shin, Y.-K. Sun, *J. Power Sources* **2006**, *159*, 1328.
[28] J. Li, L. E. Downie, L. Ma, W. Qiu, J. R. Dahn, *J. Electrochem. Soc.* **2015**, *162*, A1401.
[29] S.-U. Woo, C. S. Yoon, K. Amine, I. Belharouak, Y.-K. Sun, *J. Electrochem. Soc.* **2007**, *154*, A1005.
[30] J. Zheng, W. H. Kan, A. Manthiram, *ACS Appl. Mater. Interfaces* **2015**, *7*, 6926.
[31] S. Moitzheim, S. De Gendt, P. M. Vereecken, *J. Electrochem. Soc.* **2019**, *166*, A1.
[32] F. Mattelaer, K. Geryl, G. Rampelberg, J. Dendooven, C. Detavernier, *ACS Appl. Mater. Interfaces* **2017**, *9*, 13121.
[33] K. B. Gandrud, A. Pettersen, O. Nilsen, H. Fjellvåg, *J. Mater. Chem. A* **2013**, *1*, 9054.
[34] M. Cazorla Soult, PhD Thesis, Vrije Universiteit Brussel, **2023**.
[35] X. Zheng, X. Li, Z. Wang, H. Guo, Z. Huang, G. Yan, D. Wang, *Electrochim. Acta* **2016**, *191*, 832.
[36] S. D. Herrmann, P. K. Tripathy, S. M. Frank, J. A. King, *J. Appl. Electrochem.* **2019**, *49*, 379.
[37] A. I. Pitillas, L. L. De Taeye, P. M. Vereecken, *Adv. Mater. Interfaces* **2024**, *11*, 2400003.
[38] A. I. Pitillas Martinez, PhD Thesis, KU Leuven, **2022**.
[39] P. Kurzhals, F. Riewald, M. Bianchini, H. Sommer, H. A. Gasteiger, J. Janek, *J. Electrochem. Soc.* **2021**, *168*, 110518.
[40] C. Xu, P. J. Reeves, Q. Jacquet, C. P. Grey, *Adv. Energy Mater.* **2021**, *11*, 2003404.